Journal of Aerosol Science 193 (2026) 106760

Contents lists available at ScienceDirect

Journal of Aerosol Science

journal homepage: www.elsevier.com/locate/jaerosci

Particle image velocimetry for spray measurement of an Aerosol-on-Demand jet-printhead

Dominic Poeppe [a,*], Martin Ungerer [b], Jochen Kriegseis [a], Marc Hehner [a], Ingo Sieber [b]

[a] Institute of Fluid Mechanics (ISTM), Karlsruhe Institute of Technology (KIT), Kaiserstr. 10, Karlsruhe, 76133, Germany
[b] Institute for Automation and Applied Informatics (IAI), Karlsruhe Institute of Technology (KIT), Hermann-von-Helmholtz-Platz 1, Eggenstein-Leopoldshafen, 76344, Germany

ARTICLE INFO

Editor: Chris Hogan

Keywords:
Ultrasonic generated aerosol
Aerosol-on-demand jet-printer
Spray measurements
Velocity field measurement
Particle image velocimetry

ABSTRACT

Aerosol jet printing offers advantages over common inkjet methods for printed electronics, such as finer structures, layer homogeneity, and 3-D substrate printing capabilities. Our institute is developing a patented Aerosol-on-Demand (AoD) jet-printing process. Understanding the aerosol spray's droplet velocity fields is crucial for this development. We report on the use of the particle image velocimetry method to measure the droplet velocities and to demonstrate the on-demand capability of the AoD printing principle. The nature of the spray with very high velocity gradients on the one hand, and sparse droplet density in some regions on the other hand poses great challenges for PIV resulting in vector replacement rates of approximately 45%. Despite this, the measurements successfully quantified the maximum droplet velocities in excess of $3\,\mathrm{m\,s^{-1}}$ and demonstrated the on-demand capability, confirming a spray cessation time of approximately $50\,\mathrm{ms}$.

1. Introduction

1.1. Background

Printed electronics is an emerging market with large potential and many applications, but also many challenges. Unlike traditional subtractive manufacturing processes, additive manufacturing used in printed electronics relies on material deposited in layers. This offers unique advantages, such as reduced material waste and a high degree of process flexibility. Through the use of specialized inks with electrical, chemical, or optical properties, novel functional structures are made possible (Suganuma, 2014; Choi et al., 2015; Magdassi & Kamyshny, 2017; Das & He, 2019; Sieber et al., 2020).

Common methods for droplet-based functional printing include inkjet, aerosol jet, and electrohydrodynamic printing. In aerosol jet printing, inks are atomized into microscopic droplets, which are then accelerated and focused into a jet by a sheath gas. This focused aerosol jet is directed onto a substrate to deposit the ink. A key strength of aerosol jet printing is its highly collimated jet, which allows for a flexible nozzle-to-substrate distance of several millimeters. This capability enables printing on strongly non-planar surfaces, a significant advantage over inkjet and electrohydrodynamic printing that require small and constant nozzle-to-substrate distances (Ungerer et al., 2015; Gao, 2018; Derby, 2010; Sieber et al., 2022; Ungerer, Benítez et al., 2023).

* Corresponding author.
E-mail address: poeppe@kit.edu (D. Poeppe).

https://doi.org/10.1016/j.jaerosci.2026.106760
Received 10 November 2025; Received in revised form 19 January 2026; Accepted 5 February 2026
Available online 6 February 2026

This article concerns a novel, patented Aerosol-on-Demand (AoD) system developed at the Karlsruhe Institute of Technology (KIT) (Ungerer, Hofmann et al., 2023). In contrast to conventional aerosol jet techniques, where the ink is atomized outside of the print head, the AoD technology integrates the atomizer unit directly into the print head. Here, the functional ink is atomized inside the nozzle at the tip of a capillary, which is oscillated by a piezo actuator. This integrated design avoids long aerosol feed paths between the atomizer unit and the nozzle, while almost completely eliminating ink waste. This enables a compact system design, printing operation in all spatial directions, a widely adjustable distance between the nozzle and substrate, and jet-on-demand operation, in which the aerosol generation can be switched on and off at high frequency (Ungerer, Hofmann et al., 2023; Ungerer, 2023; Benítez, 2016).

1.2. Objective

Characterizing the velocity field is crucial for the development of the AoD atomizer unit. On the one hand, atomization currently works reliably, but not reproducibly at constant frequencies. Here, knowledge of the velocity fields can provide information about the dependence of the spray properties on the individual atomizer units. On the other hand, the velocity field makes it possible to identify the highest velocities and unfavorable angles that are most likely to incur droplet wall contacts of the inside of the nozzle of the assembled printhead. Such wall contacts would not only lead to contamination of the inner wall of the nozzle but could also lead to blockage of the nozzle outlet and thus to the failure of the printing process or unwanted ink deposition and destruction of the print (Ungerer et al., 2022). Furthermore, the velocity field is required as an inlet boundary condition for the computational fluid dynamics (CFD) model of the atomization and for the validation of the atomization model (Sieber et al., 2022; Ungerer et al., 2023c, 2024).

Specifically, we are using Ansys Fluent in its versions R19.3 and R20.1 for fluid dynamic calculations following an Euler–Lagrange approach in which the fluid phase is treated as a continuum by solving the Reynolds-averaged Navier–Stokes equations, while the dispersed phase is solved by tracking a large number of particles through the calculated flow field of the continuous phase. To predict the trajectory of a discrete phase particle the acting forces on the particle are integrated. This force balance equates the particle inertia and can be written as

$$m_p \frac{\partial \vec{u}_p}{\partial t} = m_p \frac{\vec{u} - \vec{u}_p}{\tau_r} + m_p \frac{\vec{g}(\rho_p - \rho)}{\rho_p} + \vec{F}, \tag{1}$$

where m_p is the particle mass, $\vec{u}$ is the velocity of the fluid phase, $\vec{u}_p$ is the particle velocity, ρ_p is the particle density, ρ is the density of the fluid, $\vec{F}$ are additional forces, and $m_p \frac{\vec{u}-\vec{u}_p}{\tau_r}$ is the drag force acting on the particle. To be able to model the generated aerosol in this regime, knowledge of velocity field of the droplet distribution at the capillary tip is essential, which motivates the present work.

Lastly, the start-stop behavior of the atomizer unit can be quantitatively determined by measuring the velocity fields.

A variety of optical techniques are available for the characterization of spray dynamics, each with distinct advantages and limitations. Point-wise methods like Laser Doppler Velocimetry (LDV) offer high-accuracy velocity data but are best suited for characterizing steady flows, where a velocity field can be assembled over time by traversing the measurement volume. As previous studies have shown the AoD spray to be unstable and exhibit large variations in its current configuration (Bachmann, 2023), a point-wise approach like LDV is not well-suited for capturing its instantaneous spatial structure.

Field-based techniques, such as Particle Tracking Velocimetry (PTV) and Interferometric Particle Imaging (IPI), can provide instantaneous velocity maps. IPI, in particular, offers the potential for simultaneous 3D velocity and droplet size measurements. However, its reliance on defocused particle images makes it susceptible to image overlap, limiting its application to sprays with lower droplet densities (Maeda et al., 2000; Zhuo et al., 2022). Similarly, PTV is most effective in low-density regions where individual droplets can be unambiguously tracked between frames.

Given these considerations, Particle Image Velocimetry (PIV) was selected for this initial investigation. As a well-established and robust field measurement technique, PIV is well-suited for providing a foundational, quantitative overview of the spray's velocity structure. This approach allows for a baseline characterization of the flow, establishing key velocity scales and spatial features. The insights gained from this PIV study are intended to guide further system development and inform the potential application of more specialized diagnostics in future work.

Particle Image Velocimetry (PIV) works by imaging particles that scatter light from a pulsed light source. In most applications, a flow is seeded with tracer particles for indirect velocity measurement, i.e., the particles are measured in order to infer the velocity of the seeded medium. In our problem, a direct velocity measurement is carried out, as the velocity of the microdroplet particles themselves, and not that of the surrounding medium, is of interest. The technique captures velocity and location information in two dimensions. While PIV can be expanded to three dimensions, for this initial investigation, the atomized spray is assumed to be rotationally symmetric in a first approximation, and only planar information is captured. Droplet diameter information cannot be captured using this technique and remains a question for further research. Measurement of droplet flow information using PIV is well established, with applications in similar spray systems documented in the literature (Husted et al., 2009; Estevadeordal & Goss, 2005).

The focus of this article is on three main aspects: first, the applicability of PIV measurements for the specific conditions of the AoD droplet spray; second, a preliminary evaluation of the resulting aerosol velocity fields; and third, a quantitative determination of the on-demand capability of the AoD principle. The remainder of this article is structured as follows: Section 2 describes the AoD atomizer unit and the PIV methodology. Section 3 details the experimental implementation. The results are presented and discussed in Section 4. The article concludes with a summary of the experimental results and an outlook on further developments.

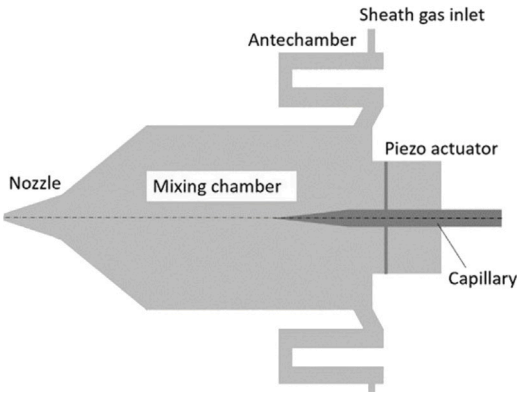

Fig. 1. Schematic of the AoD jet-printhead (Ungerer et al., 2023c). Atomizer unit in dark gray, comprised of capillary and piezo actuator. Nozzle in light gray. Only the atomizer unit is investigated in this paper. All design parameters of the nozzle can be found in Ungerer, Benítez et al. (2023).

2. Methodology

2.1. Aerosol-on-demand

In our patented Aerosol-on-Demand (AoD) jet-printing process, the ink is atomized directly within the print head. This avoids long aerosol delivery paths, enables the atomization of only small amounts of ink, and thus allows for high-frequency switching of aerosol generation as well as printing in all spatial directions. Fig. 1 shows a schematic of the AoD jet print head: the atomizer unit (dark gray) is directly integrated into the mixing chamber. In the full system, the sheath gas is introduced through four circumferential inlets of the print head. As it flows through the folded pre-chamber, the sheath gas flow is homogenized (Sieber et al., 2022). The thus homogenized sheath gas flow meets the aerosol spray in the mixing chamber and focuses the aerosol together with the nozzle geometry.

The investigations in this paper focus specifically on the aerosol generation unit itself, without the focusing nozzle and sheath gas assembly. As shown in Fig. 2, the standalone atomizer unit is connected to a function generator (Siglent SDG2122X), outputting a sine wave of frequency ranging from 100 kHz to 500 kHz and amplitude ranging from 12 V to 19 V. The large range is necessitated by the currently unreproducible atomization behavior which is subject of ongoing research. This sine wave drives a capillary into motion, atomizing the liquid at the 60 μ m tip to generate a droplet spray. A pressure control maintains a stable pressure in the reservoir to stabilize atomization. A flow rate sensor (Sensirion SLG-0150, accuracy of 5%) is installed between the reservoir and the capillary to measure the volumetric flow rate of the liquid. The volumetric flow rates tested range between $\sim$ 3000 nl/min and $\sim$ 9500 nl/min.

Ultrapure water is used in place of functional inks for reasons of ease of handling and personnel safety. While functional inks exhibit different rheological properties than ultrapure water, which ultimately affects the atomization behavior, the primary focus of this study is on the suitability of PIV as a measurement method for use with AoD atomization.

2.2. Particle image velocimetry

The principle of the PIV setup used in this paper is shown in Fig. 3. Highly collimated light from a laser is converted into a light sheet using cylindrical optics, directed through an aperture onto the droplet flow, where it is scattered by droplets. The measurements are conducted just below the tip of the capillary. The laser is pulsed in short, highly energetic pulses. Illustrative sections of two images captured in immediate succession are framed in blue at time t_0 and $t_0 + \Delta t$. Between the two points in time, a downward displacement can be observed in this illustrative example. Since the time between the two light pulses Δt is known and the scaling factor between the image and object can be calibrated, the velocity of droplet ensembles can be calculated once the displacement in pixel coordinates of the droplet images between the two pulses has been accurately determined.

2.3. Image acquisition

High-quality PIV images necessitate properly tuned image acquisition parameters. These parameters include exposure mode, light and camera timings, region of interest, particle choice, choice of light source, number of correlation pairs, camera resolution, and image calibration. For a comprehensive overview of these parameters and the mathematical principles underlying PIV, the reader is referred to Adrian and Westerweel (2011) or Raffel et al. (2018).

The image acquisition employed a standard PIV exposure mode, often referred to as double frame/single exposure. In this approach, two image frames are captured in quick succession for each PIV recording. The laser is pulsed twice, once towards the end

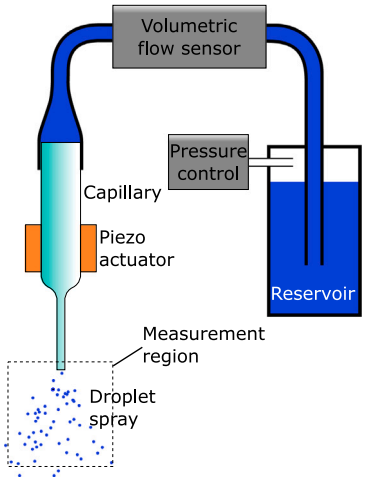

Fig. 2. Setup of the AoD atomizer unit and liquid inflow.

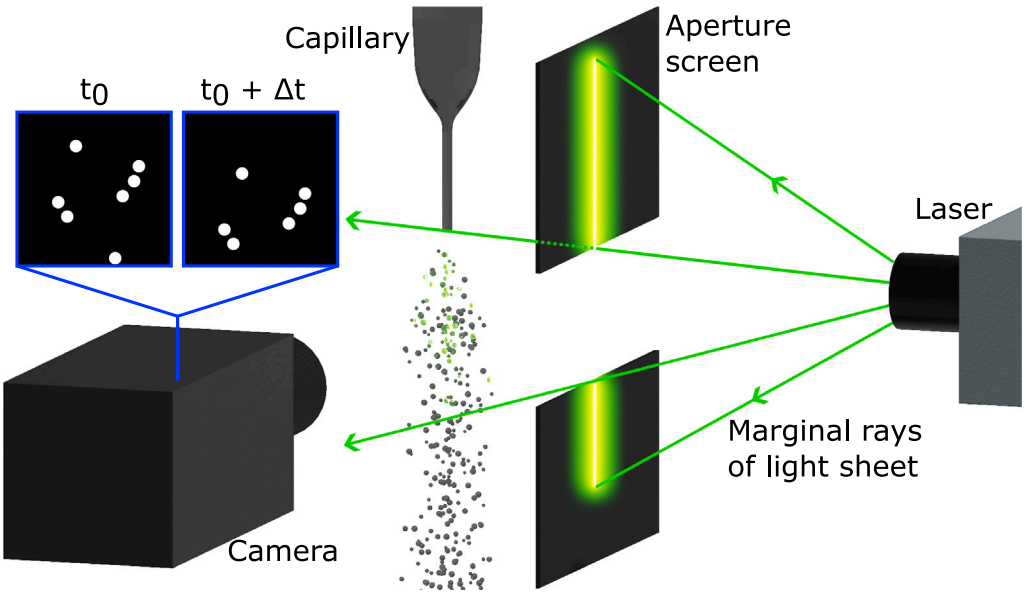

Fig. 3. Sketch of the experimental setup for Particle Image Velocimetry (PIV) used to measure the droplet spray velocity of the AoD atomizer unit.

of the exposure for the first frame (frame A) and again towards the beginning of the exposure for the second frame (frame B) of the pair. This timing strategy ensures that the effective exposure time for particle imaging is governed by the short laser pulse duration (typically < 1 μs), which minimizes motion blur for fast-moving droplets. The crucial time interval for velocity calculation, Δt, is the precisely controlled time between these two laser pulses. Displacement correlation is then performed between these consecutively captured frames A and B to determine particle displacement and subsequently the velocity field.

2.4. Image processing

Velocity fields are obtained by investigating the correlation between each frame A and frame B. The initial step involves subdividing the image into interrogation areas (IAs). The selection of IA size presents a critical trade-off in PIV analysis. On one hand, larger IAs generally yield more robust correlations due to a higher number of particle pairs and an improved signal-to-noise ratio. However, this robustness comes at the cost of spatial resolution, as larger IAs can average out small-scale flow structures. Conversely, smaller IAs offer the potential to resolve finer details in the velocity field. Yet, they are more prone to correlation errors, particularly in regions with low particle seeding density or high out-of-plane loss (droplets entering or exiting the light sheet

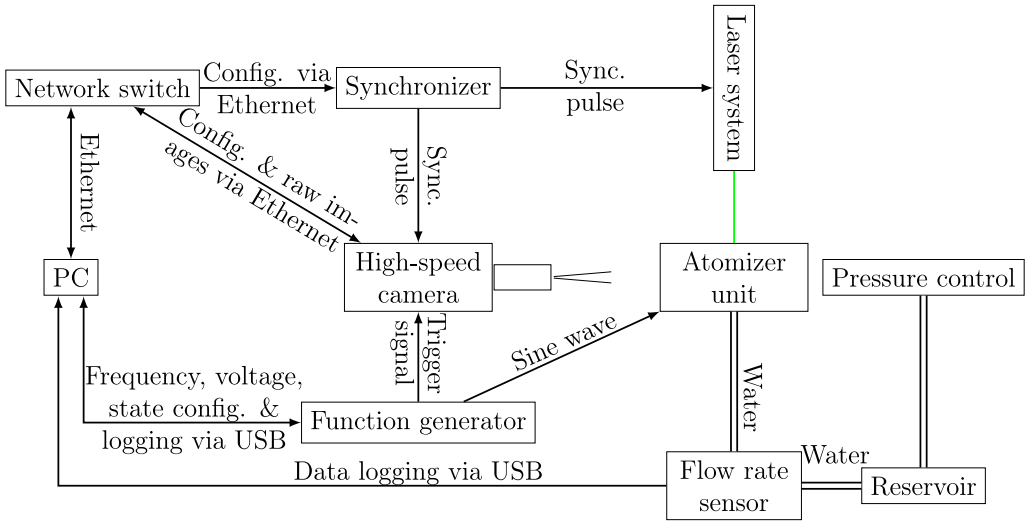

Fig. 4. Schematic of the measurement setup.

between frames). Thus, the choice of IA size requires careful consideration of these conflicting optimization parameters to balance correlation reliability with the desired level of detail in the velocity measurements. Multi-grid evaluation presents an approach where the IA size is iteratively reduced and the displacement information from previous, coarser iterations used to reduce the correlation errors of small IAs, thus improving spatial resolution while maintaining high accuracy.

By fitting a Gaussian function to the particle images, their centers can be located with sub-pixel accuracy (Raffel et al., 2018, p. 182ff.). The intensity pattern of an IA in frame A is then cross-correlated with the corresponding area in frame B to find the most probable displacement. To improve correlation accuracy in the presence of strong velocity gradients, advanced algorithms such as iterative window deformation can be employed. This technique deforms the IA in the second frame based on a predicted velocity field, which can greatly improve image matching in complex flows like the one studied here (Scarano, 2002).

3. Implementation

3.1. Setup

The schematic of the PIV setup is depicted in Fig. 4. The PC remotely controls the function generator and simultaneously records the electrical parameters of the atomizer unit and the trigger time of the high-speed camera for synchronization. The function generator simultaneously activates the atomizer unit (sine wave) and triggers the image sequence recording of the high-speed camera via two separate channels. The synchronizer provides a pulse signal with 2 kHz for the camera and a double pulse signal with 1 kHz for the laser (pulse duration ~ 100 ns) in order to accomplish the aforementioned double frame/single exposure timing.

The physical implementation of the setup is shown in Fig. 5. A Photron FASTCAM SA4 12-bit high-speed camera was used at a resolution of 512 × 512 pixels. To achieve sufficient magnification, the camera is equipped with a lens stack consisting of two Kenko Teleplus N-AF 2X DGX teleconverters and a combination of 36 mm and 20 mm intermediate rings. Illumination is provided by an Amplitude Terra PIV laser (527 nm wavelength). For each experimental condition, a series of 10,000 image pairs is recorded. The camera capture and laser output are synchronized with an iLA 5150 Synchronizer v2.

3.2. Processing parameters

The Python package OpenPIV v0.25.0 with multi-threaded processing is used for the PIV analysis. Multi-grid processing with IA sizes of 64 and 32 pixels, overlap of 50% and window deformation was chosen.

The calculated velocity fields are validated using a signal-to-noise threshold of 1.5 (peak-to-peak) (Charonko & Vlachos, 2013; Xue et al., 2014), standard deviation threshold of 7.0 (Raffel et al., 2018) and local median threshold of 3.0 (Westerweel & Scarano, 2005), where the respectively chosen thresholds have been iteratively modified towards a local optimum. Invalid vectors are replaced using a weighted average of valid neighboring velocities. In certain droplet regions, this validation process results in a high replacement rate for invalid vectors (~45%). The physical significance and methodological ramifications of this are discussed in Section 4.2.4.

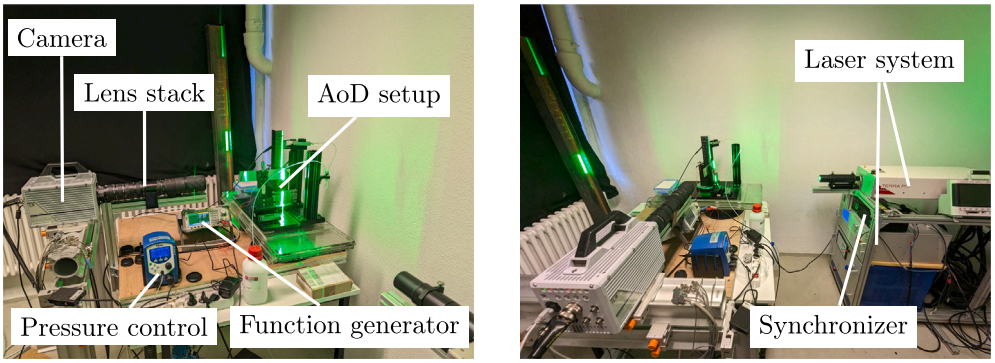

Fig. 5. Experimental setup for PIV acquisition.

4. Results and discussion

Data are collected based on atomization experiments, each of which differs in the volume flow rate of the aerosol spray generated. In this section, PIV investigations are carried out for data with an average droplet volume flow rate of 3024 nl/min (PIV-1), with a standard deviation of 255 nl/min, and 9474 nl/min (PIV-2), with a standard deviation of 183 nl/min. All experiments in this section are performed in double frame/single exposure mode and acquired with a pulse distance of 40 µs.

4.1. Convergence analysis

Convergence analysis is performed to evaluate whether and when velocity information converges to a particular value. The point of convergence is given by the number of image pairs needed to achieve a statistically significant average velocity (Raffel et al., 2018, p. 213). For this analysis, the average velocity is taken from the 3×3 IA kernel centered on the IA with the highest average velocity of the entire double image stack. The kernel velocity $\hat{u}_n$, with n being the index along the double image stack, is therefore defined as:

$$\hat{u}_n = \frac{\sum_{i=-1}^{1} \sum_{j=-1}^{1} u_{a-i,b-j,n}}{9}, \tag{2}$$

where the coordinates a, b are defined such that

$$u_{a,b} = max\left(\sum_{n=1}^{m} u_{x,y}\right), \tag{3}$$

where m is the total number of image pairs, in our case 10,000. Finally, to plot the convergence diagram, the cumulative mean velocity $\mu(k)$ is evaluated for an increasing number of image pairs k (where $k \in \mathbb{N}, 1 \leq k \leq m$) and is defined as:

$$\mu(k) = \sum_{n=1}^{k} \hat{u}_n. \tag{4}$$

In addition, the same analysis is done with the coefficient of variation, defined as $CV(k) = \frac{\sigma(k)}{\mu(k)}$, where $\sigma(k)$ is the standard deviation defined as:

$$\sigma(k) = \sqrt{\frac{\sum_{n=1}^{k} (\hat{u}_n - \mu(k))^2}{k}}. \tag{5}$$

Being a dimensionless variable, it is particularly beneficial when comparing different data sets (Raffel et al., 2018, p. 213ff.), Abdi and Williams (2010).

Fig. 6 shows the cumulative mean velocity and the coefficient of variation, both evaluated for the kernel with the highest average velocity. Significant variation is present even at high image pair counts n. While a true steady-state is not achieved within the sampled time frame, both the mean velocity and the coefficient of variation reach statistically steady values after approximately 10^3 image pairs. This indicates that the number of acquired images is sufficient for reliable ensemble averaging.

4.2. Velocity field analysis

The velocity field is presented in two manners with different objectives.

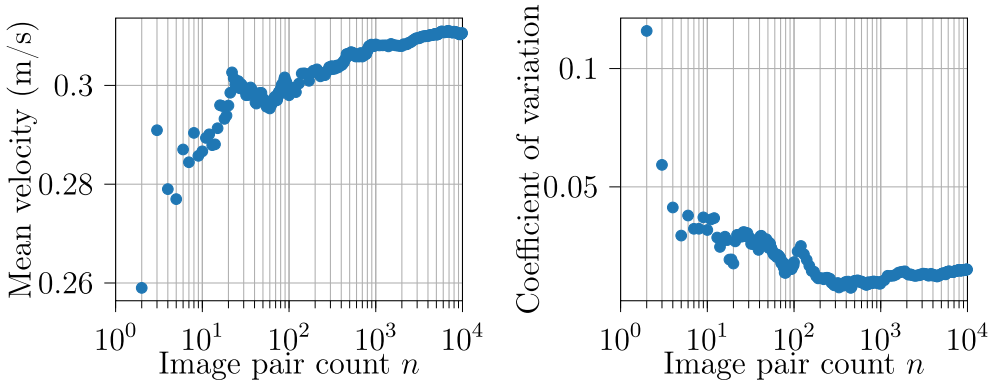

Fig. 6. Convergence analysis: mean velocity (left) and coefficient of variation (right).

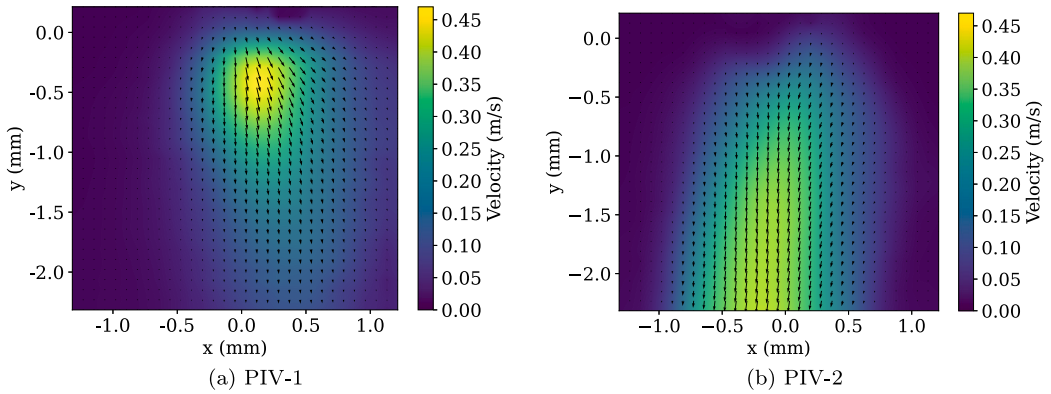

Fig. 7. Average velocity fields.

- For CFD simulation purposes and the creation of a digital twin, the average velocity field is important as a point of validation (Pfannenstiel et al., 2024).
- To ensure reliable operation, the maximum droplet velocity is of particular interest.

Naturally, the droplets posing the highest risk of wall contact are the ones with the highest velocity and the largest angle between their trajectory and the axis of rotation of the capillary (see Fig. 1). An abundance of wall contacts could lead to droplet coalescence, run-off, and eventual blockage of the nozzle outlet.

4.2.1. Average velocity field

The time-averaged velocity vectors are calculated individually for each IA. The resulting velocity fields of PIV-1 and PIV-2 are shown in Fig. 7. In the region of interest (ROI) each velocity vector indicates the average direction and velocity magnitude of droplet ensembles. The interpolated magnitude of the velocity is also shown through the color map. The capillary outlet is situated at the very top in the middle of the ROI ($x = 0$ mm, $y = 0$ mm).

4.2.2. Maximum velocity field

To determine the maximum velocity field, the greatest velocity is evaluated independently for each IA. The maximum velocity field is thus typically composed of IAs originating from many different image pairs. To reduce the effect of outliers, the average of the top 0.1% velocity vectors is used in Fig. 8 to composite the maximum velocity field, i.e., the ten largest velocities of the entire set of velocities of one IA are averaged, regardless of their position in the double image stack.

4.2.3. Discussion of PIV results

Both the average velocity field (Fig. 7(a)) as well as the maximum velocity field (Fig. 8(a)) for PIV-1 show results that partially align with intuitive expectation: high velocities directly at the capillary tip, where the aerosol is generated, and a reduction in velocity with increasing distance from the capillary tip due to viscous interaction with the surrounding air. However, a clear asymmetry can also be observed. Thus, the initial assumption of axial symmetry is disproven. This has the far-reaching consequence, that the AoD atomization in its current state cannot be assessed solely in a planar approach. A further deviation from expectations

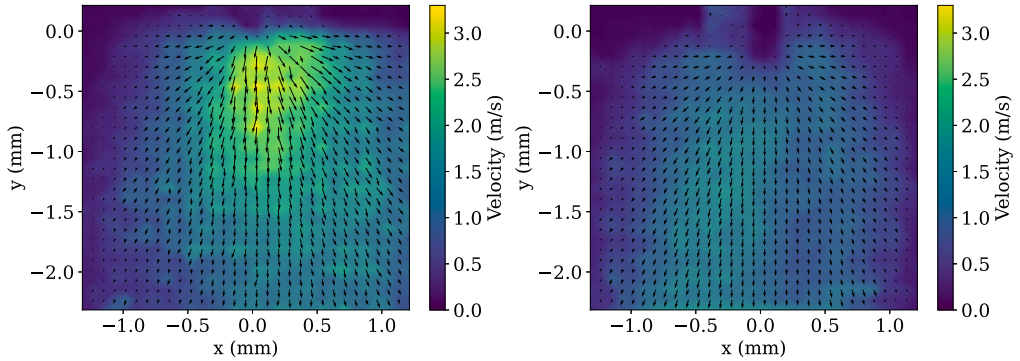

Fig. 8. Top 0.1% velocity field.

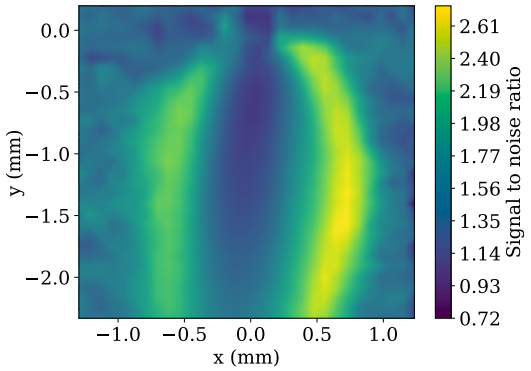

Fig. 9. Signal-to-noise ratio averaged over all image pairs of PIV-2.

can be seen in the PIV-2 velocity fields, where a reversal of the velocities can be observed: low velocities at the capillary exit and maximum velocities at the lower edge of the velocity fields (see Fig. 7(b) and Fig. 8(b)). This is particularly counter-intuitive, as the higher volumetric flow rate of PIV-2 (9474 nl/min) compared to PIV-1 (3024 nl/min) would suggest higher velocities at the capillary exit. There is no phenomenological explanation for this velocity reversal. A plausible cause is the erroneous filtering of valid high-velocity vectors near the capillary, which occurs when correlation quality is poor. The aerosol spray of the AoD exhibits a very large dynamic range of droplet velocities, with slow-moving droplets in the periphery and high-velocity droplets in the core coexisting within the same field of view. This leads to large velocity gradients that challenge the PIV correlation algorithm. Since vector replacement relies on a weighted average of neighbors, and the high-velocity region is small, the filtering process will inherently bias the results toward the lower velocities that dominate the surrounding areas.

Looking at the signal-to-noise ratio (SNR) of the PIV-2 measurement strengthens the hypothesis, that a large degree of vector filtering contributed to the unexpected velocity field. The SNR constitutes an important validation metric as mentioned in Section 3.2 and therefore has a direct impact on the results post-validation. The SNR averaged over all image pairs is depicted in Fig. 9. It is noticeable that the SNR is very low in the regions directly below the capillary. Conversely, areas with a high SNR are mainly located in the outer regions of the droplet spray, where low velocities are found. These outer regions are also where the lowest depth of the three-dimensional flow volume can be assumed, meaning that the droplets in this region are all entrained in the same flow. In contrast, the low SNR in the center of the spray can be attributed to the PIV technique integrating information over the thickness of the light sheet. It is important to note that the light sheet, while thin, has a finite thickness of approximately 1–2 mm, which is comparable to the spray's approximate diameter of 2 mm. Therefore, especially in the center of the spray, a single two-dimensional interrogation area captures droplet images from a considerable range of depths within the light sheet, which in turn can have large differences in velocities. It is recommended to decrease this thickness in future investigations using a slit aperture.

This issue of large velocity gradients and droplet overtaking can likely be alleviated by a shorter laser pulse distance (Δt). However, this introduces a trade-off. While a smaller Δt would improve correlation in high-velocity regions, it would also increase the relative measurement error in low-velocity regions, as the measured pixel displacement becomes smaller (Raffel et al., 2018).

Both Figs. 7 and 8 lead to the conclusion, that the aerosol cannot be assumed to be rotationally symmetric in any case. Therefore, the rapid droplet deceleration with increasing distance from the capillary tip in PIV-1 could be explained by the aerosol spray possessing a relatively large out-of-plane component (z-direction) so that the light sheet intersects the lower-velocity outer regions

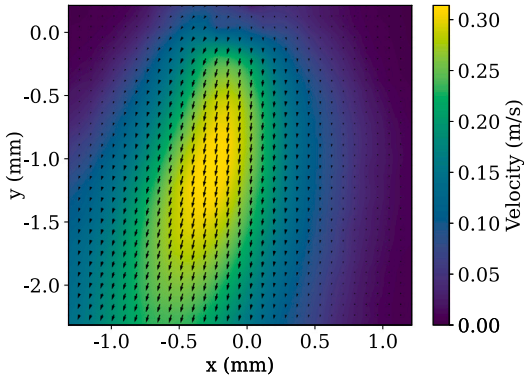

Fig. 10. PIV 3 (~ 3000 nl/ min, standard deviation of 82 nl/ min).

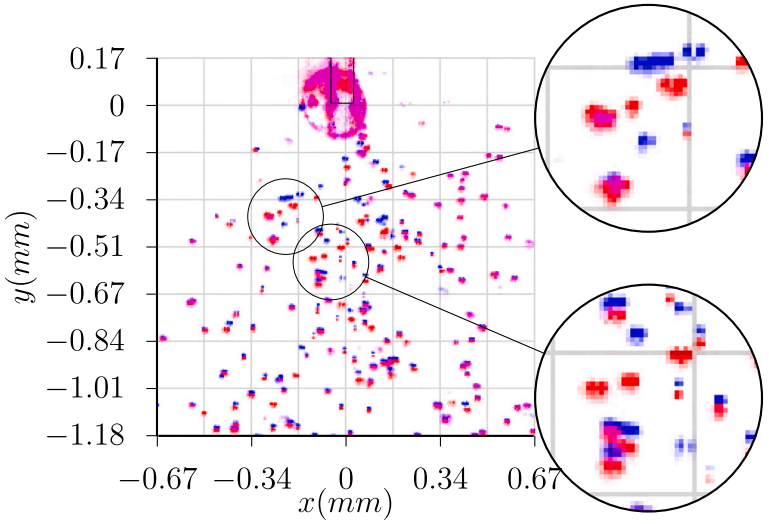

Fig. 11. Cropped section of color-coded double frame image: frame A blue, frame B red. Approximate location of the nozzle drawn in black. The grid spacing is IA size. Two sections highlighted to exemplify likely problems in the raw images.

of the spray rather than its core. This is supported by investigating an additional velocity field with the same volumetric flow rate as in PIV-1, introduced in Fig. 10 as PIV-3. The velocity field of PIV-3 does not show a similarly rapid deceleration of the droplets, while being operated at the same volumetric flow rate. If PIV-1 does exhibit significant z velocity components, the overall velocity magnitude would be underestimated due to the limitation of the setup only measuring two components and requiring the assumption of zero velocity for the third component. If the spray reliability is not improved, future studies should thus aim at a three dimensional investigation.

4.2.4. Discussion of methodology

Although PIV is a well-established and robust technique and its application to similar spray systems has also been documented, its application on the spray generated in the AoD underlies several unique challenges. The main problems arise from two properties of the AoD-generated spray:

1. High velocity gradients between droplets lead to ambiguity in image correlation.
2. Low droplet density in parts of the region of interest (ROI) gives difficulties to evaluation with imaging techniques.

Fig. 11 shows a cropped section of two overlaid color-coded frames, where frame A is colored blue and frame B is colored red. The tip of the capillary is visible at the top of Fig. 11. Overlaid is a grid with 32-pixel spacing, emulating the size of the evaluation grid used. The grid shown in Fig. 11 is only for illustration and is not the grid used for evaluation. The evaluation grid instead has an overlap of 50%.

Fig. 11 illustrates several core challenges in applying PIV to the AoD spray. The non-uniform displacement between droplets from frames A and B highlights the large velocity gradients that arise because droplets are ejected with substantially varying velocities,

rather than acting as passive tracers. This complex motion leads to several phenomena that degrade correlation quality. It is not uncommon for faster droplets to pass slower ones between frames (in-plane loss), or for droplets to exit the light sheet entirely (out-of-plane loss). Both effects, along with the chaotic droplet arrangement that can cause correlation ambiguity, lead to incorrect vector matching. E.g., Fig. 11 top detail section shows multiple frame A droplets (blue) at the top, which cannot be definitively correlated to a matching frame B droplet (red). Similarly, the bottom detail section shows multiple frame B droplets without a matching frame A droplet, likely due to out-of-plane loss. While the use of window deformation mitigates the problem of a high-velocity gradient, it does not resolve these correlation issues. Furthermore, Fig. 11 also shows droplets that appear pink. This color-mixture indicates very small displacements between droplets from different frames. These low-velocity regions could have been resolved better with a larger laser pulse distance, highlighting the difficulty in selecting a single Δt that is optimal across the entire high-dynamic-range flow field.

In addition, when looking at the droplet density, it is noticeable that there are many grid areas without any droplet images making correlation impossible. Moreover, a large part of the main flow area has a very low droplet density, which increases the correlation uncertainty leading to a larger degree of filtering. These problems are particularly evident in velocity fields calculated from individual image pairs, which underscores the need for averaging velocity fields over a large set of image pairs to achieve statistical significance.

In conclusion, while the issue of droplet overtaking could be improved by reducing the laser pulse distance, it should be noted that a shorter pulse distance increases the error in the low-velocity regions and does not improve the fundamental problem of large velocity gradients between droplets of the same IA. Instead, this could, in theory, be alleviated using smaller IAs, though in practice the low droplet density of the AoD will likely limit the benefits. This underlines the need to very carefully tune the capture and processing parameters for measuring the AoD spray or similar applications.

The problem of axial non-symmetry, unless eradicated through an improved atomizer unit, could result in the need for three component velocity measurement techniques.

4.3. Start-stop behavior

One of the key advantages of AoD over commercial aerosol jet printers is the ability to rapidly activate and deactivate the droplet spray generation by switching of the voltage supply to the atomizer unit. To characterize the start-stop dynamics of the system, a series of images was captured in high-speed multi-image mode at a frame rate of 10 kHz (pulse interval of 100 µs), i.e., continuous capture with constant laser pulse to camera offset, meaning each image can be correlated with its subsequent image. During the image acquisition, the atomizer unit's driving voltage was momentarily interrupted and shortly thereafter reactivated. The velocity field is analyzed as a moving average, computed over 50 image pairs with a temporal resolution of 3.33 ms. Simultaneously, the volumetric flow rate of the spray was recorded using the flow rate sensor introduced in Section 2.1 to establish a correlation between the velocity field and the flow rate. Figs. 12 and 13 show selected velocity fields alongside the volumetric flow rate data. The red marker in the flow rate graph denotes the point in time corresponding to the displayed velocity field. The final velocity field prior to voltage interruption (Fig. 12(a)) reveals a uniform droplet flow with a sensor-recorded volumetric flow rate of 2700 nl/min. 6.66 ms after voltage deactivation at the atomizer unit (Fig. 12(b)), faster droplets have already exited the ROI, though no change in the measured volumetric flow rate is observed.

A further 46.6 ms later (Fig. 13(a)), the slowest droplets have exited the ROI and the velocity is uniformly zero, yet the measured volumetric flow rate still displays no significant change. Following voltage reactivation at the atomizer unit, a uniform flow pattern re-emerges within 46.6 ms (Fig. 13(b)), as evidenced by the velocity field. In contrast, the flow rate sensor exhibited a delay of approximately 0.7 seconds before detecting a change in mass flow, a lag likely attributable to the sensor's operating principle or data transmission latency.

5. Conclusions

The objective of this study is to establish the suitability of PIV as a measurement method for use with the AoD atomizer unit and to gather quantitative data on the atomization. The key differentiating factor of AoD, the on-demand functionality, was quantitatively confirmed, demonstrating a rapid spray cessation time of approximately 50 ms. The preliminary evaluation of the velocity fields revealed a highly unsteady and non-symmetrical flow structure, pointing to fundamental problems of the current atomizer unit design, which need to be addressed in future works. The evaluation presented also identified maximum velocities exceeding $3\,\mathrm{m\,s^{-1}}$ at a wide range of ejection angles. From this, problematic parameter settings that are likely to lead to wall contact can be derived. The large variation in results between individual experiments highlights the current challenge of achieving reproducible atomization. A future comprehensive parameter study, guided by these initial findings, is therefore warranted. Finally, it is concluded that while PIV is suitable for a largely qualitative basic characterization, its application with regard to quantitative results is challenging due to the specific properties of the spray; specifically, the high dynamic range and low seeding density resulted in low signal-to-noise ratios and vector replacement rates of up to 45% in the high-velocity regions.

The greatest challenges for PIV are the high velocity gradients between droplets and the sparse droplet distribution, which results in a low signal-to-noise ratio and correlation ambiguities. The discovery of a strong three-dimensional flow structure further highlights the limitations of a 2D planar measurement approach. Consequently, while the results provide valuable qualitative insights, the current data quality is not sufficient to serve as a robust basis for use in computational fluid dynamics (CFD) simulations. This remains a future goal of the velocity field evaluation.

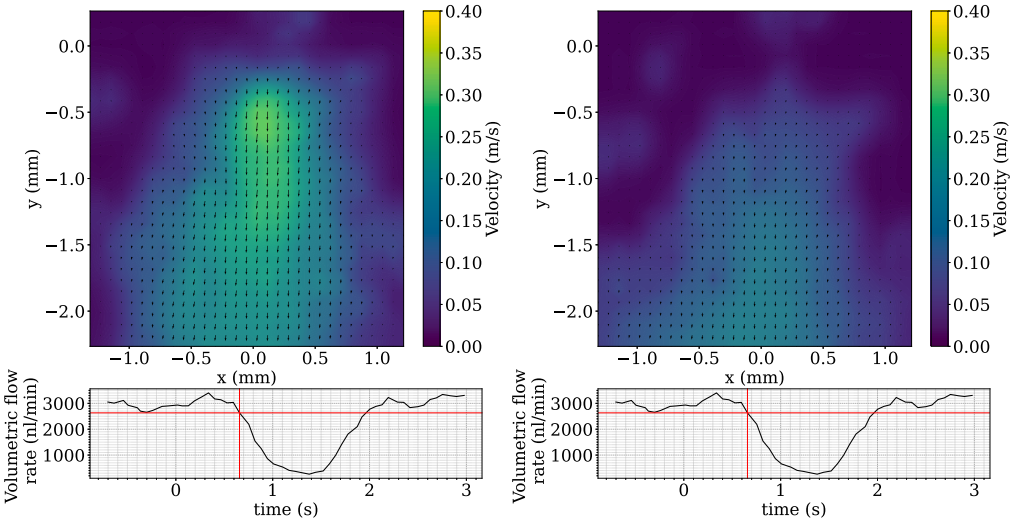

(a) Frame 191, 637 ms (b) Frame 193, 643 ms

Fig. 12. Moving average of 50 image pairs, frames 191 and 193.

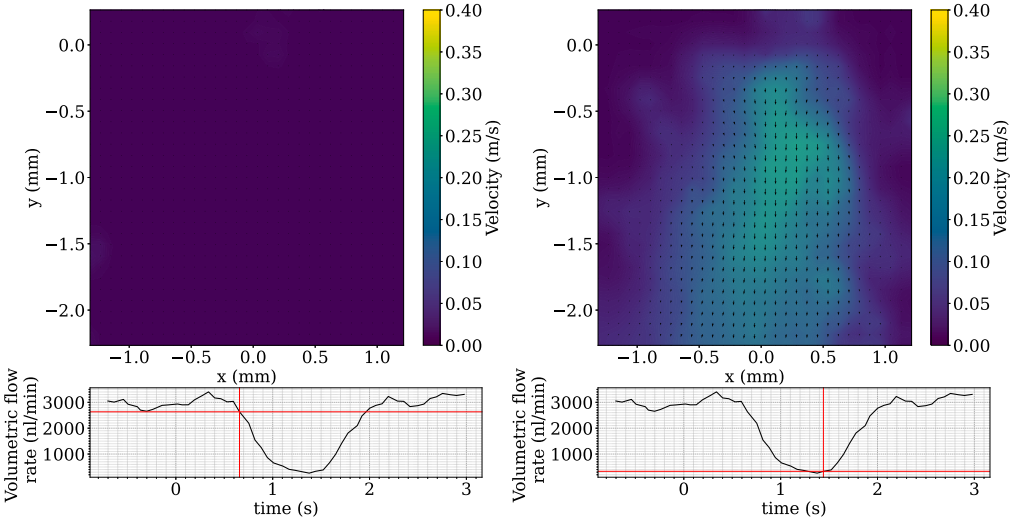

(a) Frame 207, 690 ms (b) Frame 440, 1467 ms

Fig. 13. Moving average of 50 image pairs, frames 207 and 440.

To overcome these limitations, the use of more advanced three-dimensional diagnostic methods is planned in future work. Shake-the-Box (STB), a time-resolved Lagrangian Particle Tracking (LPT) method, is a particularly promising candidate since it tracks individual particles in 3D space through a temporal sequence of images (Schanz et al., 2016). Its application offers the potential not only to resolve the observed 3D flow structures but also to provide the high-fidelity Lagrangian data necessary for a deeper physical understanding of the atomization process.

CRediT authorship contribution statement

Dominic Poeppe: Writing – review & editing, Writing – original draft, Visualization, Software, Methodology, Investigation, Data curation, Conceptualization. **Martin Ungerer:** Writing – review & editing, Supervision, Resources, Project administration, Methodology, Investigation, Funding acquisition, Formal analysis, Conceptualization. **Jochen Kriegseis:** Writing – review & editing, Methodology, Investigation, Conceptualization. **Marc Hehner:** Investigation, Data curation. **Ingo Sieber:** Writing – review & editing, Supervision, Resources, Project administration, Methodology, Investigation, Funding acquisition, Formal analysis, Conceptualization.

Declaration of competing interest

The authors declare that they have no known competing financial interests or personal relationships that could have appeared to influence the work reported in this paper.

Acknowledgments

This work was supported by the program Materials Systems Engineering of the Helmholtz Association.

Data availability

Data will be made available on request.

References

Abdi, H., & Williams, L. (2010). *Coefficients of correlation, alienation, and determination* (pp. 175–180). Sage.

Adrian, R. J., & Westerweel, J. (2011). Particle image velocimetry. In *Cambridge aerospace series*: *No. 30*, Cambridge Univ. Press.

Bachmann, M. V. (2023). *Untersuchungen zur Hydrophobierung der Zerstäubereinheit eines Aerosol-on-Demand Jet-Druckkopfes [Studies on hydrophobic coatings of the atomizer unit of an Aerosol-on-Demand jet printhead]* (Bachelor's Thesis), Karlsruhe: Karlsruhe Institute of Technology, Institute for Automation and Applied Informatics.

Benítez, J. L. (2016). *Fluiddynamische Simulation hinsichtlich der Fokussierung eines Aerosolstroms [Fluid dynamic simulation with regard to the focussing of an aerosol flow]* (Bachelor's Thesis), Karlsruhe: Karlsruhe Institute of Technology, Institute for Automation and Applied Informatics.

Charonko, J. J., & Vlachos, P. P. (2013). Estimation of uncertainty bounds for individual particle image velocimetry measurements from cross-correlation peak ratio. *Measurement Science and Technology*, *24*, Article 065301. http://dx.doi.org/10.1088/0957-0233/24/6/065301.

Choi, H. W., Zhou, T., Singh, M., & Jabbour, G. E. (2015). Recent developments and directions in printed nanomaterials. *Nanoscale*, *7*, 3338–3355. http://dx.doi.org/10.1039/C4NR03915G.

Das, R., & He, X. (2019). Flexible, printed and organic electronics 2020–2030: forecasts, technologies, markets. URL: https://www.idtechex.com/en/research-report/flexible-printed-and-organic-electronics-2020-2030-forecasts-technologies-markets/687.

Derby, B. (2010). Inkjet printing of functional and structural materials: Fluid property requirements, feature stability, and resolution. *Annual Review of Materials Research*, *40*, 395–414. http://dx.doi.org/10.1146/annurev-matsci-070909-104502.

Estevadeordal, J., & Goss, L. (2005). Piv with led: Particle shadow velocimetry (psv). In *43rd AIAA aerospace sciences meeting and exhibit - meeting papers*. http://dx.doi.org/10.2514/6.2005-37.

Gao, J. G. Z. Dajing (2018). Designs and applications of electrohydrodynamic 3d printing. *International Journal of Biosciences*, *5*, 172. http://dx.doi.org/10.18063/ijb.v5i1.172.

Husted, B. P., Petersson, P., Lund, I., & Holmstedt, G. (2009). Comparison of PIV and PDA droplet velocity measurement techniques on two high-pressure water mist nozzles. *Fire Safety Journal*, *44*, 1030–1045. http://dx.doi.org/10.1016/j.firesaf.2009.07.003.

Maeda, M., Kawaguchi, T., & Hishida, K. (2000). Novel interferometric measurement of size and velocity distributions of spherical particles in fluid flows. *Measurement Science and Technology*, *11*, L13–L18. http://dx.doi.org/10.1088/0957-0233/11/12/101.

Magdassi, S., & Kamyshny, A. (2017). *Nanomaterials for 2D and 3D printing*. Weinheim: Wiley-VCH.

Pfannenstiel, H., Ungerer, M., & Sieber, I. (2024). Digital twin architecture to use for optimizing an aod-printing process. In *2024 symposium on design, test, integration and packaging of MEMS/MOEMS*. IEEE, http://dx.doi.org/10.1109/DTIP62575.2024.10613180.

Raffel, M., Kähler, C. J., Kompenhans, J., Scarano, F., Wereley, S. T., & Willert, C. E. (2018). *Particle image velocimetry: a practical guide* (3rd ed., 2018th ed.). Cham: Springer International Publishing and Imprint: Springer.

Scarano, F. (2002). Iterative image deformation methods in PIV. *Measurement Science and Technology*, *13*, R1–R19. http://dx.doi.org/10.1088/0957-0233/13/1/201.

Schanz, D., Gesemann, S., & Schröder, A. (2016). Shake-the-box: Lagrangian particle tracking at high particle image densities. *Experiments in Fluids*, *57*, 70. http://dx.doi.org/10.1007/s00348-016-2157-1.

Sieber, I., Thelen, R., & Gengenbach, U. (2020). Assessment of high-resolution 3d printed optics for the use case of rotation optics. *Optics Express*, *28*, 13423–13431. http://dx.doi.org/10.1364/OE.391697.

Sieber, I., Zeltner, D., Ungerer, M., Wenka, A., Walter, T., & Gengenbach, U. (2022). Design and experimental setup of a new concept of an aerosol-on-demand print head. *Aerosol Science and Technology*, *56*, 355–366. http://dx.doi.org/10.1080/02786826.2021.2022094.

Suganuma, K. (2014). Introduction to printed electronics. In *springerBriefs in electrical and computer engineering*: *Vol. 74*, New York, NY: Springer, http://dx.doi.org/10.1007/978-1-4614-9625-0.

Ungerer, M. (2023). *Neue Methodik zur Optimierung von Druckverfahren für die Herstellung funktionaler Mikrostrukturen und hybrider elektronischer Schaltungen* (Ph.D. thesis), Karlsruhe Institute of Technology.

Ungerer, M., Benítez, J. L., Zeltner, D., Wenka, A., Gengenbach, U., & Sieber, I. (2023). Modelling and design-for-manufacturing of an aerosol-on-demand jet-printhead. In G. Wagner, F. Werner, & F. De Rango (Eds.), *Simulation and modeling methodologies, technologies and applications* (pp. 1–21). Cham: Springer International Publishing.

Ungerer, M., Gengenbach, U., Hofmann, A., & Bretthauer, G. (2015). Comparative and systemic analysis of digital single nozzle printing processes for the manufacturing of functional microstructures,vergleichende untersuchung und systemische betrachtung verschiedener digitaler ein-düsen-druckverfahren zur herstellung funktionaler mikrostrukturen. *MikroSystemTechnik Kongress 2015 MEMS Mikroelektronik Systeme Proceedings*, 441–444.

Ungerer, M., Hofmann, A., Scharnowell, R., Gengenbach, U., Sieber, I., & Wenka, A. (2023). Druckkopf und druckverfahren [print head and printing method]. (p. 103). Patent: EP 3 752 365 B1.

Ungerer, M., Walter, T., & Sieber, I. (2023). Position analysis of the atomiser unit of an aerosol-on-demand jet-printhead by means of computational fluid dynamics. In *Proceedings of the 13th international conference on simulation and modeling methodologies, technologies and applications* (pp. 126–133). Rome, Italy: SCITEPRESS - Science and Technology Publications, http://dx.doi.org/10.5220/0012131000003546.

Ungerer, M., Walter, T. P., & Sieber, I. (2024). Tolerancing of the atomiser unit of an aerosol-on-demand jet-printhead. In *Simulation and modeling methodologies, technologies and applications*. Cham: Springer, http://dx.doi.org/10.1007/978-3-031-77603-8_4.

Ungerer, M., Zeltner, D., Wenka, A., Gengenbach, U., & Sieber, I. (2022). Modelling and simulation of an aerosol-on-demand print head with computational fluid dynamics. In *Proceedings of the 12th international conference on simulation and modeling methodologies, technologies and applications* (pp. 44–51). SCITEPRESS - Science and Technology Publications, http://dx.doi.org/10.5220/0011258100003274.

Westerweel, J., & Scarano, F. (2005). Universal outlier detection for piv data. *Experiments in Fluids*, *39*, 1096–1100. http://dx.doi.org/10.1007/s00348-005-0016-6.

Xue, Z., Charonko, J. J., & Vlachos, P. P. (2014). Particle image velocimetry correlation signal-to-noise ratio metrics and measurement uncertainty quantification. *Measurement Science and Technology*, *25*, Article 115301. http://dx.doi.org/10.1088/0957-0233/25/11/115301.

Zhuo, Z., Wu, Y., Wen, B., Lin, Z., & Wu, X. (2022). Modeling and experiment on 3D position and size measurement of opaque droplet cloud with astigmatic dual-beam interferometric particle imaging (ADIPI). *Powder Technology*, *395*, 111–121. http://dx.doi.org/10.1016/j.powtec.2021.09.025.